Possibility of fully spin-polarized nodal chain state in several spinel half metals

Haopeng Zhang,[1,2] Xiaoming Zhang,[1,2,*] Ying Liu,[2,3] Xuefang Dai,[1,2] Guang Chen,[4] and Guodong Liu[1,2,†]

[1]*State Key Laboratory of Reliability and Intelligence of Electrical Equipment, Hebei University of Technology, Tianjin 300130, China*
[2]*School of Materials Science and Engineering, Hebei University of Technology, Tianjin 300130, China*
[3]*Research Laboratory for Quantum Materials, Singapore University of Technology and Design, Singapore 487372, Singapore*
[4]*Baoding Fengfan Rising Battery Separator Co., Ltd., Baoding 071052, Hebei province, People's Republic of China*

Nodal-chain fermions, which are novel topological states of matter, have been hotly discussed in the field of nonmagnetic materials. Here, by using first-principles calculations and symmetry analysis, we propose the realization of a fully spin-polarized nodal chain in several spinel half metals, including LiV_2O_4, VMg_2O_4, $FeAl_2O_4$, and $NiAl_2O_4$. In these materials, the ferromagnetic state takes on a half-metal band structure, and only the bands from the single channel are present near the Fermi level. Taking LiV_2O_4 as an example, we show how the crossing of bands in the spin-up channel forms two types of nodal loops. These nodal loops arise from band inversion and are under the protection of the glide mirror symmetries. Remarkably, we find that the nodal loops join with each other and form a chainlike nodal structure. Correspondingly, the ω-shaped surface states are also fully spin-polarized. The fully spin-polarized nodal chain identified here has not been proposed in realistic materials before. An effective model is constructed to describe the nature of the nodal chain. The effects of the electron correlation, the lattice strains, and the spin-orbit coupling are discussed. The fully spin-polarized bulk nodal chain and the associated nontrivial surface states for a half metal may pave the way for additional applications in spintronics.

I. INTRODUCTION

Topological semimetals have attracted a tremendous amount of attention recently because of their potential applications in various fields. They also provide a feasible bridge to investigate the novel characteristics of high-energy particles [1–10]. In topological semimetals, the crossings between valence and conduction bands can show different dimensionalities, thus different types of topological semimetals can be formed with hosting nodal points (such as Dirac/Weyl points) [11–18], nodal lines [19–25], and nodal surfaces [26–29]. Nodal lines have many nodal structures. For example, one single nodal line can either traverse the whole Brillouin zone (BZ) or form a closed loop without penetrating the BZ, as distinguished by the Z^3 index [30]. For another example, a nodal line can be classified as type-I, type-II, critical-type, or hybrid line according to the slope of the crossing bands [30–33]. In addition, when multiple nodal lines coexist in the Brillouin zone, they can form different configurations, such as crossing loops, a nodal net, a nodal box, a Hopf link, and a nodal chain [34–43]. Recently, nodal-chain semimetal has been hotly discussed [39,40,44–52]. They contain a chain of connected loops in momentum space, and the connecting points are under the protection of special symmetries.

Compared with their nonmagnetic counterparts, magnetic topological semimetals are attracting increasing attention at

present because they are special in several aspects. From a fundamental physics point of view, time-reversal symmetry (TRS) is broken in a magnetic system. For example, TRS-breaking Weyl semimetals are distinct, and to some degree they are simpler than inversion-symmetry-breaking semimetals due to their nonzero anomalous Hall conductivity. In addition, there is the potential to contain at least one pair of Weyl points in the Brillouin zone [53–61]. Also, the symmetry is dependent on the magnetization direction in a magnetic system. As a result, an alternative topological phase transition may result from shifting the magnetic symmetry, which is controlled by an external magnetic field [62–65]. Magnetic topological semimetals are also desirable from an application point of view because they have the potential to be applied in spintronic devices. A series of magnetic topological semimetals with variable fermionic states have been proposed [66–69]. In an ideal situation, the topological fermions have 100% spin-polarization, and such fermions are termed topological half metals. The compounds $HgCr_2Se_4$ [70] and $Co_3Sn_2S_2$ [53] are examples of Dirac/Weyl half metals; $Li_3(FeO_3)_2$ [71], tetragonal β-V_2PO_5 [62], and MnN monolayer [72] are examples of nodal loop half metals; and $CsCrX_3$ ($X =$ Cl, Br, I) are examples of nodal surface half metals [29]. Unfortunately, we have not seen any reports on nodal chain half metals. Previously, nodal chains were mostly proposed in nonmagnetic materials [39,46–52]. The Heusler compound Co_2MnGa is almost the only example of a magnetic nodal chain semimetal composed of multiple types of nodal chains [40]. Unfortunately, this material is not a half metal, and the transports for nodal chains are not fully spin-polarized. Thus, it is highly desirable to explore a nodal chain

*zhangxiaoming87@hebut.edu.cn
†gdliu1978@126.com

195124-1

half metal that is composed of a fully spin-polarized nodal-chain fermion.

In the present work, we report on several existing spinel compounds, including LiV_2O_4, VMg_2O_4, $FeAl_2O_4$, and $NiAl_2O_4$, which are all nodal chain half metals. The band structures of these compounds exhibit insulating properties in one spin channel, and metallic properties in the other. Using the ferromagnetic (FM) state of LiV_2O_4 as a prototype system, we study the band topology of these spinel half metals. In LiV_2O_4, the conduction and valence bands in the spin-up channel cross with each other, which generates a fully spin-polarized nodal chain. The nodal chain is made from two types of nodal loops, and it is protected by the glide mirror symmetries. We built an effective model that well describes the mechanism of a nodal chain. Furthermore, the nodal chain is found to be robust against electron correlation effects and lattice strain. The spin-orbit coupling (SOC) effect on the nodal chain is discussed. This work suggests that these spinel half metals are a good material platform through which to investigate the fundamental physics of nodal-chain fermions in ferromagnets.

II. METHODS

In this work, we perform first-principles calculations by using the Vienna ab initio Simulation Package (VASP) [73], based on density functional theory (DFT) [74]. The valence electron configurations of Li $(2s^1)$, V $(3d^34s^2)$, O$(2s^22p^4)$, Mg $(3s^2)$, Fe $(3d^64s^2)$, Al $(3s^23p^1)$, and Ni $(3d^84s^2)$ are applied, and the projector augmented wave method is adopted for the interaction between the valence electrons and the ionic core potentials [74]. During calculations, the cutoff energy is set as 600 eV. The Brillouin zone is sampled by a Monkhorst-Pack k-mesh with a size of $15\times15\times15$. To optimize the lattice of these spinel compounds, the force and energy convergence criteria are applied as 0.01 eV/Å and 10^{-6} eV, respectively. To account for the correlation effects for V, the GGA+U method is applied to describe the Coulomb interaction [75]. The effective U values for V, Fe, and Ni are set as 4 eV to investigate the topological band structure, and the conclusions will not change when the U values are slightly shifted. The irreducible representations of the electronic states are obtained by using the IRVSP code [76]. The surface states are calculated by using the WANNIERTOOLS package [77].

III. CRYSTAL AND MAGNETIC STRUCTURES

The spinel compounds LiV_2O_4, VMg_2O_4, $FeAl_2O_4$, and $NiAl_2O_4$ focused on in this work have similar crystal and band structures; hence, in the following we take LiV_2O_4 as an example to investigate the band topology. The LiV_2O_4 compound is an existing material, and it was synthesized as early as 1960 [80]. In former experiments, LiV_2O_4 crystals were synthesized via different methods. For example, polycrystalline samples of LiV_2O_4 can be synthesized via a solid-state reaction from the starting materials Li_3VO_4, V_2O_3, and V_2O_5 [78]. Recently, single crystals of LiV_2O_4 were successfully grown using the flux method at the 69:26:5 molar ratio of $LiCl/Li_2MoO_4/LiBO_2$ [79]. In particular, the grown single crystals of LiV_2O_4 can possess both high quality
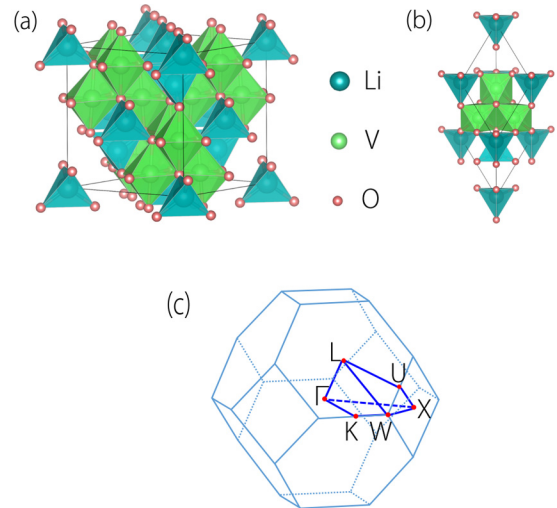

FIG. 1. (a) The conventional and (b) the primitive unit cell of crystal structure for LiV_2O_4. (c) The corresponding Brillouin zone with the considered high-symmetry paths.

and large size, which greatly favor their further experimental characterizations. It crystallizes in a normal spinel structure with the nonsymmorphic space group $Fd\bar{3}m$ (No. 227). Figure 1(a) shows the crystal structure of LiV_2O_4. In the crystal structure, the bonding between V and O atoms forms a V-O_6 octahedral local structure, and the bonding between Li and O atoms forms an Li-O_4 tetrahedral local structure. The cubic unit cell contains 56 atoms, with 32 O atoms occupying the $32e$ (u, u, u) Wyckoff position, 16 V atoms at the $16d$ (0.5, 0.5, 0.5) Wyckoff position, and 8 Li atoms at the $8a$ (0.125, 0.125, 0.125) Wyckoff position. One unit cell contains four primitive cells, and the primitive cell formed from LiV_2O_4 is shown in Fig. 1(b). After lattice optimization, the optimized value for "u" is 0.261, and the ground lattice constants are $a = b = c = 8.465$ Å, in good agreement with former computational and experimental values [80–82]. In the following band-structure calculations, we apply the optimized lattice structure. Note that the conclusions of this work will not change when the experimental structure is applied.

Because of the unoccupied d shells in the transition-metal V element, there may be a magnetism moment in LiV_2O_4. Here we determine the ground magnetic configuration by comparing the total energies among different magnetic states, which include ferromagnetic (FM), nonmagnetic (NM), and antiferromagnetic (AFM) states. In each magnetic state, we have considered the three magnetization directions with the highest potential in the cubic system, including the [001], [110], and [111] directions. The obtained energies for all the magnetic configurations are summarized in Table I. It can be clearly found that $FM_{[001]}$ has the lowest energy. Therefore, from our calculations, the ground magnetic configuration of LiV_2O_4 is FM, and the magnetic moment ordering is along the [001] direction. We have also estimated the ground magnetic state of VMg_2O_4, $FeAl_2O_4$, and $NiAl_2O_4$, and we found that the FM states have the lowest energy among different magnetic configuration. The calculated results are consistent with the experimental results [83,84]. High-quality $FeAl_2O_4$ samples synthesized with urea exhibit typical ferromagnetic

TABLE I. Total energy E_{tot} per unit cell (in eV, relative to that of the FM_{001} ground state), as well as magnetic moment M (in units of μ_B) per V atom. The values are calculated by the GGA+SOC method with $U = 4.0$ eV.

	FM_{001}	FM_{110}	FM_{111}	AFM_{001}	AFM_{110}	AFM_{111}
Energy/eV	0	0.243	0.187	0.199	0.296	0.285
M_x/μ_B	0.001	1.103	0.922	0.044	1.086	0.889
M_y/μ_B	0.001	1.122	0.912	0.034	1.089	0.888
M_z/μ_B	1.570	0.019	0.882	1.537	0.015	0.882

behavior [83]. $NiAl_2O_4$ exhibits weak ferromagnetic behavior [84]. VMg_2O_4 was reported very recently to be a ferromagnetic half-metal [61].

IV. WEYL NODAL CHAIN WITHOUT SOC

The electronic band structures of LiV_2O_4 in the absence of SOC are shown in Figs. 2(a) and 2(b). The spin-resolved band structures exhibit two features. First, the bands in the spin-up channel exhibit a metallic character with two bands crossing the Fermi level, whereas those in the spin-down channel exhibit an insulating character with a big band gap of 3.27 eV. These results indicate that LiV_2O_4 is a half metal, where the conduction electrons are fully spin-polarized. Second, in the spin-up channel, the two bands near the Fermi level cross with each other and form several band crossings in the K-W, W-Γ, Γ-X, and X-L paths. We will show later that these band crossings form nodal chains in the BZ. In Figs. 2(a) and 2(b), we also show the total and projected density of states (TDOSs and PDOSs) of LiV_2O_4. The TDOSs and PDOSs clearly show that the electron states near the Fermi level are mostly contributed by the d orbitals of V.
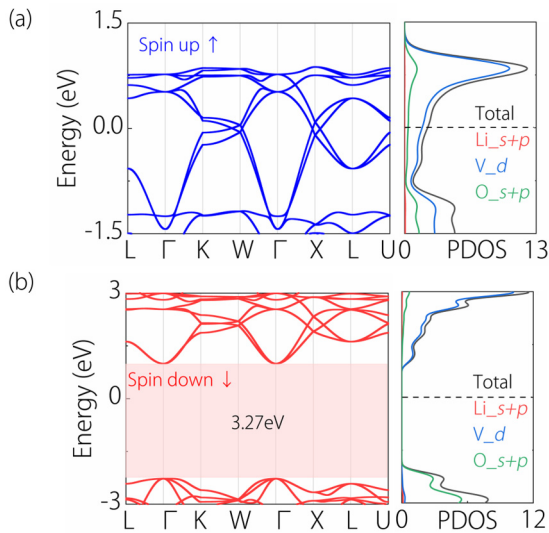

FIG. 2. The electronic band structures and projected density of states (PDOS) of LiV_2O_4 compound in the absence of SOC. Part (a) is for the spin-up ones, showing a metallic character with two bands crossing the Fermi level. Part (b) is for the spin-down channel, showing an insulating character with a big band gap of 3.27 eV.
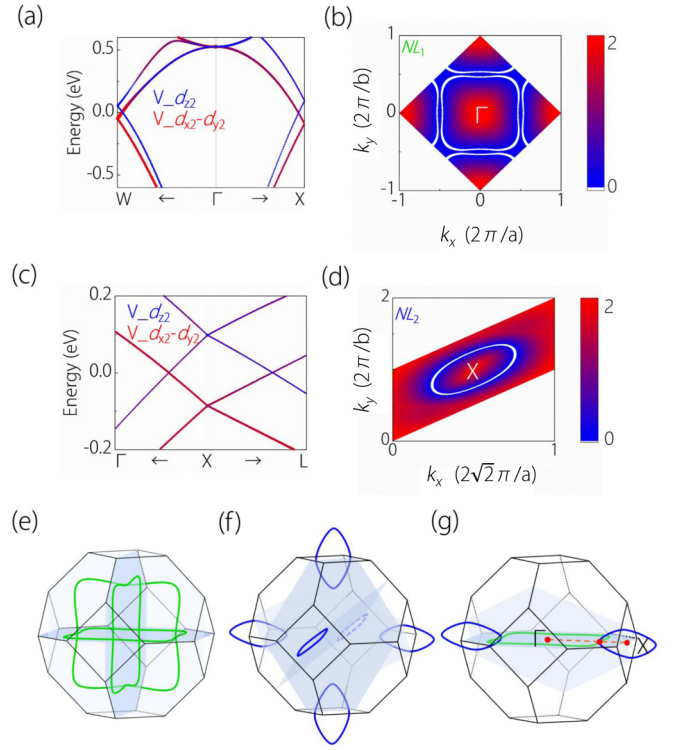

FIG. 3. (a) and (c) Orbital-projected band structure of LiV_2O_4, including V-d_{z^2} orbital (blue) and V-$d_{x^2-y^2}$ orbital (red). Parts (b) and (d) show the nodal loops in the $k_z = 0$ plane and the Γ-X-L plane, which are labeled as NL_1 and NL_2, respectively. Parts (e) and (f) are schematic illustrations of the NL_1 and NL_2 in the Brillouin zone, respectively. (g) The schematic illustrations of the nodal chain in LiV_2O_4. The green and blue lines in (e) and (f) denote NL_1 and NL_2, respectively.

We have also calculated the band structure of other spinel materials including VMg_2O_4, $FeAl_2O_4$, and $NiAl_2O_4$ (see Fig. 7). They are also half-metals that possess crossing points in one spin channel, and semiconducting or insulating gaps in the other spin channel. For VMg_2O_4, a crossing points is shown in the K-W, W-Γ, Γ-X, and X-L paths. However, the spin-down channel has a large gap of 4.58 eV. Different from the band structures of LiV_2O_4 and VMg_2O_4, $FeAl_2O_4$ and $NiAl_2O_4$ exhibit multiple linear crossings in the spin-down channel near the Fermi level, while in the spin-up channel there are large gaps of 3.36 and 3.96 eV, respectively. The band crossings in these compounds exhibit similar features, which will be discussed below.

Here, we use LiV_2O_4 as an example. We focus on the band structure in the spin-up channel. As displayed in Fig. 2(a), there are a total of four band crossing points near the Fermi level, which happen in the K-W, W-Γ, Γ-X, and X-L paths, respectively. After a careful scan of the band structures, we find that the crossings in the K-W, W-Γ, and Γ-X paths belong to a nodal loop in the $k_z = 0$ plane. In Fig. 3(a), we show an enlarged view of orbital-component band structures in the W-Γ and Γ-X paths. We can observe that the bands with V-d_{z^2} and V-$d_{x^2-y^2}$ orbital components are inverted, which indicates the potential nontrivial band topology in LiV_2O_4. These crossing points are not isolated but are located on a nodal loop

in the $k_z = 0$ plane. The profile of the nodal loop is shown in Fig. 3(b). This nodal loop is in fact under the protection of the glide mirror symmetry $G_z : (x, y, z) \rightarrow (x + 1/4, y + 3/4, -z + 1/2)$. This requires that the crossing bands possess opposite eigenvalues, which has been confirmed by our DFT calculations. Our calculations show that the two crossing bands have eigenvalues of $+1$ and -1, respectively. In the following, we denote this nodal loop as NL_1. Noticing the cubic symmetry of LiV_2O_4, there also exists a nodal loop in both the $k_x = 0$ and $k_y = 0$ planes. These nodal loops cross each other and form inner nodal chain structures, as shown in Fig. 3(e).

The band crossings in the Γ-X and X-L paths are also not isolated but belong to another nodal loop in the Γ-X-L plane. Figure 3(c) show the enlarged orbital-component band structures in the Γ-X and X-L paths. A profile of the nodal loop in the Γ-X-L plane is shown in Fig. 3(d). Being similar to the nodal loop in the $k_z = 0$ plane, this nodal loop is also protected by a glide mirror symmetry. The symmetry can be denoted as $G_{110} : (x, y, z) \rightarrow (-y + 1/4, -x + 3/4, z + 1/2)$. We find that the crossing bands have opposite mirror eigenvalues of ± 1. In the following, we denote this nodal loop as NL_2. According to the symmetry, there are a total of three pairs of such nodal loops in the Brillouin zone, as shown in Fig. 3(f). Very interestingly, we find that NL_1 and NL_2 are not isolated but share the same nodal point in the Γ-X path, thereby forming the nodal chain structure. The profile of the nodal chain is shown in Fig. 3(g). It can be seen that LiV_2O_4 and VMg_2O_4 form nodal chains in the spin-up channel, while $FeAl_2O_4$ and $NiAl_2O_4$ form nodal chains in the spin-down channel, and these compounds are fully spin-polarized.

Previously, nodal chains were mostly proposed in non-magnetic materials, including iridium tetrafluoride (IrF_4) [39], WC-type HfC [47], some hexagonal materials [49,85–87], ternary Li_2XY (X = Ca, Ba; Y = Si, Ge) compounds [50], metallic-mesh photonic crystal [51], and carbon networks [48]. In these examples, the spin polarization for the nodal-chain electrons is zero. Chang *et al.* reported the first example of a magnetic nodal chain in Heusler Co_2MnGa [40]. However, the electron states from both spin-up and spin-down channels are coupled near the Fermi level, thus the conducting electrons near the nodal chain are only partially spin-polarized in Co_2MnGa. In this regard, the nodal-chain state in LiV_2O_4 is different from all the nodal-chain materials proposed previously, because LiV_2O_4 is a half metal, and the conducting electrons for the nodal chain are fully spin-polarized. Such a nodal-chain half metal is very likely to have applications in spintronics for high-speed information storage and processing.

Here we investigate the surface band structure of LiV_2O_4. The equienergy slice at the Fermi level in the (001) surface is shown in Fig. 4(b). We can observe several regions of drumhead surfaces states. To clarify the origin of these states, we show the profiles of nodal chains projected on the (001) surface. As shown in Fig. 4(c), loops NL_1 and NL_2 from the chain are shown in different colors. In Fig. 4(c), we map the profiles of a projected nodal chain in the equienergy slice. We find all the drumhead surfaces states originating from the nodal chain. Furthermore, we travel across the surface Brillouin zone along two typical paths [cut1 and cut2 in Fig. 4(b)], along which we
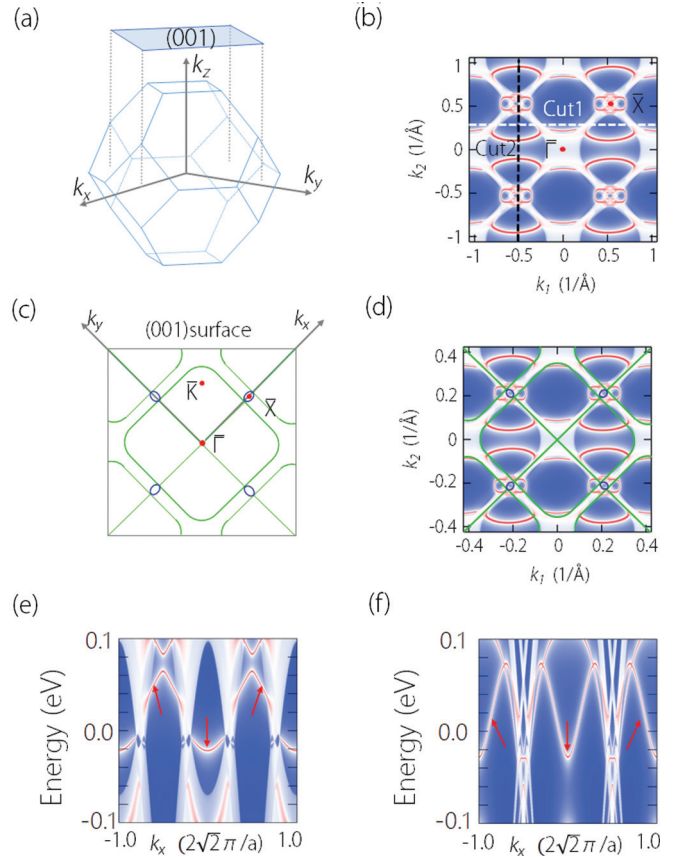

FIG. 4. (a) The bulk Brillouin zone and the projection onto the (001) surface. (b) Surface states on the (001) surface at the Fermi level. The sharp features are surface states, whereas the white region are projections of bulk bands. (c) Schematic illustration of the projection of the nodal chain on the (001) surface. (d) (001) surface states with the profiles of the projected nodal chain shown in the figure. Parts (e) and (f) are surface band structures along the white and black cuts indicated in (b), where surface states connecting adjacent band crossings are observed.

expect to cross the nodal loops several times. Corresponding surface band structures are shown in Figs. 4(e) and 4(f). We indeed observe that all of the surface states are connected by the adjacent band crossings, and they form ω-shaped surface states. Such surface states are typical features of a nodal-chain fermion [40].

V. EFFECTIVE MODEL

At the Γ point, the symmetry is characterized by the C_{4v} point group. The generators can be chosen as $\{C_{4z}, M_y, C_{2z}\}$. One should note that in the FM case, the spin-up and spin-down are decoupled in the absence of SOC. The FM term just resembles the on-site potential for a spinless system, which preserves all the original symmetries (in the absence of FM), including time-reversal symmetry $\mathcal{T}$, with $\mathcal{T} = \mathbf{K}$, where $\mathbf{K}$ is the complex conjugate. A minimal model for this two-band crossing around the Γ point can be generally written as

$$\mathcal{H}_\Gamma(k) = \varepsilon_0(k) + \sum_{i=x,y,z} d_i(k)\sigma_i, \qquad (1)$$

where $\varepsilon_0(\mathbf{k})$ is the overall energy shift, which can be neglected in our case, σ is the Pauli matrix, and $d_i(\mathbf{k})$ is the function of vector k. The time-reversal symmetry requires that

$$\mathcal{T}\mathcal{H}(\mathbf{k})\mathcal{T}^{-1} = \mathcal{H}(-\mathbf{k}), \tag{2}$$

such that d_y is an odd function of $\boldsymbol{k}$, and $d_{x,z}$ is an even function of $\boldsymbol{k}$. Generally, one has d_i in the form

$$d_{x,z} = a_0 + a_1^{x,z}k_x^2 + a_2^{x,z}k_y^2 + a_3^{x,z}k_z^2$$
$$+ c_1^{x,z}k_xk_y + c_2^{x,z}k_yk_z + c_3^{x,z}k_xk_z, \tag{3}$$

$$d_y = b_1k_x + b_2k_y + b_3k_z. \tag{4}$$

For the mirror symmetry $M_y : (x, y, z) \rightarrow (x, -y, z)$, one has

$$M_y\mathcal{H}(k_x, k_y, k_z)M_y^{-1} = \mathcal{H}(k_x, -k_y, k_z). \tag{5}$$

Furthermore, from the DFT calculations, it is shown that the low-energy states at the Γ point belong to the following irreducible representations: $\{B_i, B_2\}$. The basis functions can be chosen as $\{x^2 - y^2, xy\}$ such that $M_y = \sigma_z$. This requires that $d_z(\mathbf{k})$ is an even function of k_y; terms linear to k_yk_x, k_yk_z vanish. Then $d_z(\mathbf{k}) = a_0 + a_1^zk_x^2 + a_2^zk_y^2 + a_3^zk_z^2 + c_3^zk_xk_z$, and $d_{x,y}(\mathbf{k})$ is only the odd function of k_y. Therefore, $d_x(k) = c_1^xk_xk_y + c_2^xk_yk_x$ under the constraints from both $\mathcal{T}$ and M_y, and $d_y = b_2k_y$.

In the basis $\{B_i, B_2\}$, $C_{2z} : (x, y, z) \rightarrow (-x, -y, z)$ is an identical matrix. It requires that the Hamiltonian must be an even function of k_x and k_y, and it can also be proportional to k_xk_y. d_y therefore vanishes in the presence of the Hamiltonian. Additionally, term linear to k_xk_z vanish as well due to a negative sign arising from the C_{2z} operation. Now, one has

$$d_x = c_1^xk_xk_y, \ d_y = 0, \ d_z = a_0 + a_1^zk_x^2 + a_2^zk_y^2 + a_3^zk_z^2. \tag{6}$$

In this basis, $C_{4z} : (x, y, z) \rightarrow (-y, x, z)$, it can be written as $C_{4z} = -\sigma_0$. It requires coefficients of a term that is an odd function of k_x and k_y, and that have opposite signs but the same absolute value. It also requires coefficients of a term proportional to even order of k_x and k_y that are the same. Furthermore, the term $d_x = c_1^xk_xk_y$ disappears due to a negative sign after the operation. Therefore, the effective Hamiltonian at the Γ point can be written as

$$H(\boldsymbol{k}) = [a_0 + a_1(k_x^2 + k_y^2) + a_3k_z^2]\sigma_z. \tag{7}$$

This shows a nodal loop on the plane $k_z = 0$.

The same discussion can be applied to the nodal loop on the plane $k_y = 0$ encircling the X point. One has checked that the little group at the X point is C_{2v}, which is generated by a twofold rotation operation C_{2z} and mirror operation M_y. The general form of the Hamiltonian can be written as

$$\mathcal{H}_M(k) = \varepsilon_M(k) + \sum_{i=x,y,z} f_i(k)\sigma_i. \tag{8}$$

The same argument is applied in the presence of $\mathcal{T} = \mathbf{K}$. Hence, the function $f_i(\boldsymbol{k})$ can be given by

$$f_{x,z} = \alpha_0 + \alpha_1^{x,z}k_x^2 + \alpha_2^{x,z}k_y^2 + \alpha_3^{x,z}k_z^2$$
$$+ \gamma_1^{x,z}k_xk_y + \gamma_2^{x,z}k_yk_z + \gamma_3^{x,z}k_xk_z, \tag{9}$$

$$f_y = \beta_1k_x + \beta_2k_y + \beta_3k_z. \tag{10}$$

The irreducible representations for this little group are A_2 and B_2, and the basis can then be taken in the form $\{xy, yz\}$. As such, $C_{2z} = \sigma_z$, which requires that $f_z(\boldsymbol{k})$ is an even function of k_x and k_y, which can also be the function of $\gamma_1^zk_xk_y$. This asserts that $f_{x,y}$ is an odd function of k_x, k_y, such that

$$f_x = \gamma_1^xk_xk_z + \gamma_2^xk_yk_z, \tag{11}$$

$$f_y = \beta_1k_x + \gamma_2k_y. \tag{12}$$

In this basis, $M_y = -\sigma_i$, it is required that $f_i(\boldsymbol{k})$ must be an even function of k_y, such that when considering all of the generators, one has

$$f_x(\mathbf{k}) = \gamma_1^xk_xk_z, \ f_y(\mathbf{k}) = \beta_1k_x, \tag{13}$$

$$f_z(\mathbf{k}) = \alpha_0 + \alpha_1^zk_x^2 + \alpha_2^zk_y^2 + \alpha_3^zk_z^2. \tag{14}$$

Finally, the Hamiltonian is

$$\mathcal{H} = (\alpha_0 + \alpha_1^zk_x^2 + \alpha_2^zk_y^2 + \alpha_3^zk_z^2) + \gamma k_xk_z\sigma_x + \beta k_x\sigma_y. \tag{15}$$

It shows a nodal loop on the plane $k_x = 0$ that is described as

$$f_z(0, k_y, k_z) = \alpha_0 + \alpha_2k_y^2 + \alpha_3k_z^2. \tag{16}$$

We have proven that there are two types of nodal loops in LiV_2O_4, as shown in Figs. 3(e) and 3(f). The nodal loops touch each other at one point along the Γ-M direction and form the nodal-chain structure in the Brillouin zone, as shown in Fig. 3(g). Here, we want to point out that the effective model shown above is constructed from symmetry, thus it can also be applied to other spinel materials such as VMg_2O_4, $FeAl_2O_4$, and $NiAl_2O_4$.

VI. ROBUSTNESS OF THE NODAL CHAIN AND THE SOC EFFECT

To ensure the fully spin-polarized nodal chain, two conditions need to be considered: first, a band gap is required in the spin-up channel, which enables the half-metallic character; second, the band crossings in the spin-down channel are necessary, as they ensure the presence of a nodal chain.

To show the robustness of the spin-polarized nodal chain in LiV_2O_4, we have examined the electronic band structure against the electron correlation effects and lattice strains. In Fig. 5(a), we show the positions at the bottom of the conduction band and at the top of the valence band versus the U values of V. We can see that the band gap between the conduction band and the valence band in the spin-down channel always exists with the U values shifting from 0 to 6 eV. For the spin-up channel, the conduction and valence bands cross with each other. We find that such band crossings always remain during the shift of U values. In Fig. 5(b), we show the band structure of LiV_2O_4 in the spin-up channel with U at 6 eV. The band crossings produce the fully spin-polarized nodal chain. Moreover, we have also investigated the electronic band structure under hydrostatic strains. As shown in Fig. 5(c), we find that the band gap in the spin-down channel can retain under $\pm 5\%$ hydrostatic strain (where "+" represents tensile strain and "−" represents compressive strain). Meanwhile, the band crossings in the spin-up channel can also retain in the period. Figure 5(d) shows the band structure in the spin-up channel under a 5% tensile strain, where band crossings for a
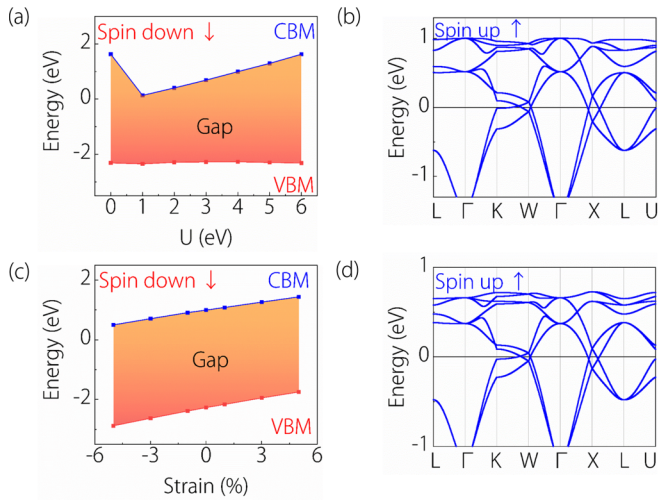
FIG. 5. (a) In the spin-down channel, the curves of the valence-band maximum (VBM) and the conduction-band minimum (CBM) are under different U values. The area formed by the curve shows the band gap in the spin-down channel. (b) The band structure of LiV_2O_4 compound in the spin-up channel with U at 6 eV. (c) The curves of VBM and CBM under different strains in the spin-down channel. (d) The spin-up band structure under a 5% tensile strain.

nodal chain are observed. These results suggest that the fully spin-polarized nodal chain in LiV_2O_4 is very robust, which may be meaningful for its future detection in experiments.

Finally, we discuss the SOC effect on the electronic band structure. The resulting band structure under SOC is shown in Fig. 6(a). We can see that the bands from both spin channels join together under SOC, but the band details do not change much near the Fermi level. As has been discussed above, NL_1 and NL_2 of the nodal chain are protected by specific
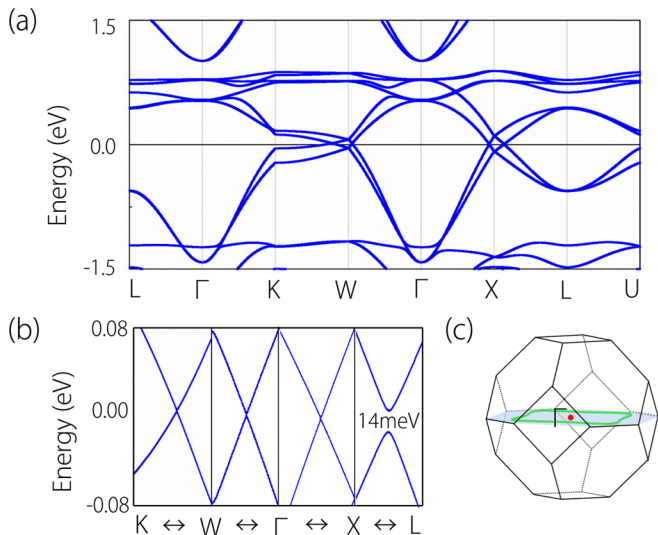

FIG. 6. (a) Electronic band structure of LiV_2O_4 under SOC with magnetization along the [001] direction. (b) The enlarged band structures in the K-W, W-Γ, and Γ-X paths are not gapped under SOC, whereas that in the X-L path is gapped with the gap size of 14 meV. (c) Schematic illustration of a single nodal loop under SOC in the $k_z = 0$ plane under the [001] magnetization.

glide mirror symmetries. In LiV_2O_4, the ground magnetic moment ordering is along in the [001] direction. All the glide mirror symmetries except G_z will be broken under such a magnetization direction. As a result, most of the loops for the nodal chain will be gapped under SOC. However, one of the NL_1 in the $k_z = 0$ plane would remain because the crossing bands still have opposite G_z eigenvalues ($\pm i$), as protected by the glide mirror symmetry G_z. These arguments have been verified by our DFT calculations. As shown by the enlarged band structures in Fig. 6(b), we can see that the band crossings in the K-W, W-Γ, and Γ-X paths are not gapped under SOC, but the band crossing in the X-L path is gapped with a gap size of $\sim$14 meV. These results have shown that LiV_2O_4 exhibits a single nodal loop under SOC, as displayed in Fig. 6(c).

We want to point out that most nodal chains identified so far will be gapped under SOC. The SOC gap in LiV_2O_4 (14 meV) is larger than that in Co_2MnGa (1 meV) [40], and it is comparable with those in Li_2XY (X = Ca, Ba; Y = Si, Ge) (18 meV) [50] and carbon networks (10–20 meV) [48], but lower than those in PtO_2 (31 meV) [45], HfC ($>$30 meV) [47], and LiAuSe ($>$30 meV) [49]. Considering the negligible SOC gap, it is very likely that the nodal chain structure will be observable in future experiments.

VII. DISCUSSION AND CONCLUSION

Before ending this paper, we make the following remarks. First, in the above sections, we use the band structure of LiV_2O_4 in the FM state to show the appearance of a fully spin-polarized nodal chain state in spinel half metals. Note that LiV_2O_4 is a heavy-fermion material. Its magnetic configuration is complex, and it is still a matter of debate. Several computational studies have focused on the mechanism of heavy fermions and magnetic states in LiV_2O_4 by using various calculation approaches [88–92]. In particular, Ali *et al.* systematically studied the electronic structure and magnetic properties of LiV_2O_4 based on the PBEsol-GGA functional plus the mBJ potential [81]. Their calculations show that the ground state of LiV_2O_4 is ferromagnetic with a half-metal band structure. These results are consistent with our calculation. Recently, Gong *et al.* came to a different conclusion, i.e., they suggested that LiV_2O_4 has a frustrated antiferromagnetic (AFM) configuration [93]. This may arise from the fact that in the LiV_2O_4 system the FM and AFM states are competing, thus its magnetic state is sensitive to computational treatments. In fact, the competition between FM and AFM states in LiV_2O_4 has already been observed in experiments. A neutron scattering experiment performed by Krimmel and colleagues showed dramatic magnetic response changes around 40 K, which characterized LiV_2O_4 as a metal with ferromagnetic order at that state [94]. Furthermore, Takeda and colleagues indeed verified the crossover region from a FM to an AFM state by NMR measurements [95]. Considering these facts, the experimental detection of nodal chain states in LiV_2O_4 is most likely to be realized in the FM region above 40 K.

It is worth noting that DFT calculations characterizing topological band structure have gained success in several heavy-fermion materials. $CeRu_4Sn_6$ is one of the most typical examples. $CeRu_4Sn_6$ has been well identified as a heavy-fermion material by experiments [96–100]. Remarkably,

Sundermann and colleagues reported that $CeRu_4Sn_6$ is a heavy-fermion material with a topologically nontrivial band structure based on both experiments and DFT calculations [99]. They found that the DFT results agree well with their experimental data. More recently, Xu and colleagues [101] reported a heavy Weyl fermion state in $CeRu_4Sn_6$ based on DFT calculations. Their findings are also consistent with the experimental results as discussed in Ref. [99]. LiV_2O_4 proposed herein is another potential topological candidate in heavy-fermion materials.

Finally, we want to point out that, among these spinel compounds, LiV_2O_4 is not the best choice to study nodal chain states because of the unclear ground magnetic configuration. Interestingly, we find that the fully spin-polarized nodal chain signature also appears in other spinel half metals, including VMg_2O_4, $FeAl_2O_4$, and $NiAl_2O_4$. In particular, the FM state of $FeAl_2O_4$ and $NiAl_2O_4$ has already been verified by previous experiments [83,84]. For $FeAl_2O_4$ spinel, magnetic measurements show a FM state at room temperature [83]. $NiAl_2O_4$ exhibits a weak ferromagnetism in magnetic measurements. The experiments on $NiAl_2O_4$ show a narrow hysteresis loop where the saturation magnetization (M_s), the remanent magnetization (M_r), and the coercivity (H_c) are 64.96×10^{-3} emu/gm, 1.825×10^{-3} emu/gm, and 67.25 Oe, respectively [84]. Even though the FM state is not intrinsic, strong magnetism may still be induced by an external magnetic field. As shown in Figs. 7(a)–7(f), these materials show half-metal band structures similar to that of LiV_2O_4. We can observe that they all show several band crossings near the Fermi level in a single spin channel (spin-up in VMg_2O_4, spin-down in $FeAl_2O_4$ and $NiAl_2O_4$). Although they show different band details, these band crossings can also form the fully spin-polarized nodal chain structure from our symmetry analysis. In these example, the nodal chains in LiV_2O_4 and VMg_2O_4 are located in the spin-up channel, while those in $FeAl_2O_4$ and $NiAl_2O_4$ are located in the spin-down channel.

In conclusion, we have demonstrated the presence of a fully spin-polarized nodal chain in several existing spinel half metals, which include LiV_2O_4, VMg_2O_4, $FeAl_2O_4$, and $NiAl_2O_4$. These materials have half-metal band structures with a metallic character in one spin channel but an insulating one in the other spin channel. In the spin channel with a metallic band structure, the materials show several band crossings near the Fermi level. Using LiV_2O_4 as the example, we show that the band crossings form two types of Weyl nodal loops, which join with each other at a specific point. This gives rise to the formation of the nodal chain structure. The nodal chain exists only in one single spin channel; hence, it is fully spin-polarized. We find that the nodal chain displays ω-shaped surface states, which are also fully spin-polarized. We further find that the nodal chain is very robust against the electron correlation effects and the lattice strain. This work provides
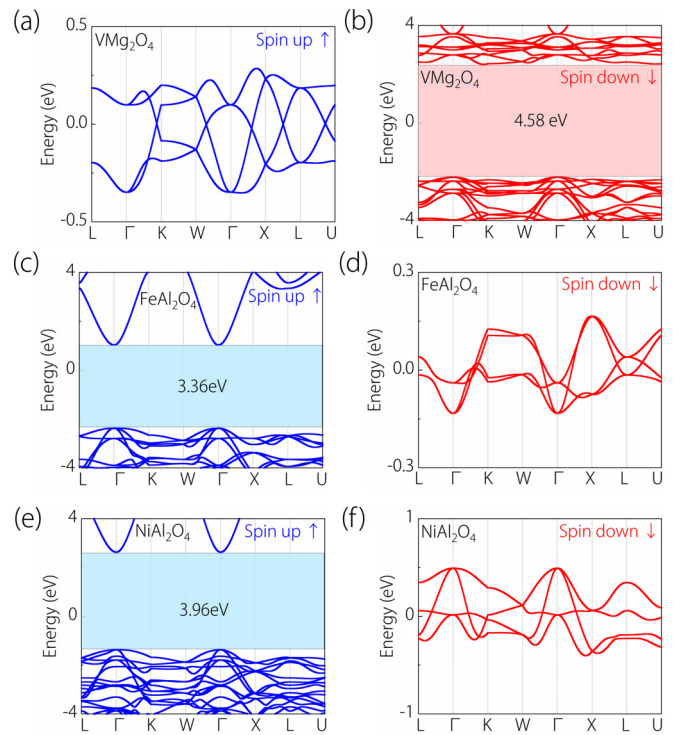

FIG. 7. Approximate Weyl semimetal phase observed in VMg_2O_4, $FeAl_2O_4$, and $NiAl_2O_4$. Part (a) is for the spin-up channel of VMg_2O_4, which is different from $FeAl_2O_4$ and $NiAl_2O_4$ in that there are multiple band crossings near the Fermi level. Part (b) is the spin-down channel band structure of VMg_2O_4, which has a band gap of 4.58 eV greater than that of $FeAl_2O_4$ and $NiAl_2O_4$. Part (c) is for the spin-up channel of $FeAl_2O_4$, showing an insulating character with a large band gap of 3.36 eV. Part (d) is for the spin-down channel of $FeAl_2O_4$, showing a metallic character with two bands crossing the Fermi level. Part (e) is for the spin-up channel of $NiAl_2O_4$, which has a band gap of 3.96 eV. Part (f) is for the spin-down channel of $NiAl_2O_4$, shown as half-metallic.

an excellent platform through which to investigate fully spin-polarized nodal chain fermions in realistic materials, and it may lead to promising applications in spintronics.

[1] A. A. Soluyanov, D. Gresch, Z. Wang, Q. Wu, M. Troyer, X. Dai, and B. A. Bernevig, Nature (London) **527**, 495 (2015).

[2] C.-K. Chiu, J. C. Y. Teo, A. P. Schnyder, and S. Ryu, Rev. Mod. Phys. **88**, 035005 (2016).

[3] A. Bansil, H. Lin, and T. Das, Rev. Mod. Phys. **88**, 021004 (2016).

[4] S. A. Yang, SPIN **06**, 1640003 (2016).

[5] A. A. Burkov, Nat. Mater. **15**, 1145 (2016).

[6] X. Dai, Nat. Phys. **12**, 727 (2016).

[7] B. Bradlyn, J. Cano, Z. Wang, M. G. Vergniory, C. Felser, R. J. Cava, and B. A. Bernevig, Science **353**, aaf5037 (2016).

[8] A. Politano, L. Viti, and M. S. Vitiell, APL Mater. **5**, 035504 (2017).

[9] P. Z. Liu, R. W. James, and J. C. Judy, Nat. Rev. Mater. **4**, 479 (2019).

[10] X.-L. Sheng, C. Chen, H. Liu, Z. Chen, Z.-M. Yu, Y. X. Zhao, and S. A. Yang, Phys. Rev. Lett. **123**, 256402 (2019).

[11] W. Meng, X. Zhang, T. He, L. Jin, X. Dai, Y. Liu, and G. Liu, J. Adv. Res. **24**, 523 (2020).

[12] X. Wan, A. M. Turner, A. Vishwanath, and S. Y. Savrasov, Phys. Rev. B **83**, 205101 (2011).

[13] S. Murakami, New J. Phys. **9**, 356 (2007).

[14] S. Borisenko, Q. Gibson, D. Evtushinsky, V. Zabolotnyy, B. Büchner, and R. J. Cava, Phys. Rev. Lett. **113**, 027603 (2014).

[15] H. Weng, C. Fang, Z. Fang, B. A. Bernevig, and X. Dai, Phys. Rev. X **5**, 011029 (2015).

[16] C. Chen, S.-S. Wang, L. Liu, Z.-M. Yu, X.-L. Sheng, Z. Chen, and S. A. Yang, Phys. Rev. Mater. **1**, 044201 (2017).

[17] N. P. Armitage, E. J. Mele, and A. Vishwanath, Rev. Mod. Phys. **90**, 015001 (2018).

[18] L. Jin, X. Zhang, Y. Liu, X. Dai, L. Wang, and G. Liu, Phys. Rev. B **102**, 195104 (2020).

[19] C. Fang, H. M. Weng, X. Dai, and Z. Fang, Chin. Phys. B **25**, 117106 (2016).

[20] S. A. Yang, H. Pan, and F. Zhang, Phys. Rev. Lett. **113**, 046401 (2014).

[21] H. Weng, Y. Liang, Q. Xu, R. Yu, Z. Fang, X. Dai, and Y. Kawazoe, Phys. Rev. B **92**, 045108 (2015).

[22] Y. Chen, Y. Xie, S. A. Yang, H. Pan, F. Zhang, M. L. Cohen, and S. Zhang, Nano Lett. **15**, 6974 (2015).

[23] T. He, X. Zhang, Y. Liu, X. Dai, G. Liu, Z.-M. Yu, and Y. Yao, Phys. Rev. B **102**, 075133 (2020).

[24] Z.-M. Yu, W. Wu, X.-L. Sheng, Y. X. Zhao, and S. A. Yang, Phys. Rev. B **99**, 121106(R) (2019).

[25] L. Jin, X. Zhang, Y. Liu, X. Dai, X. Shen, L. Wang, and G. Liu, Phys. Rev. B **102**, 125118 (2020).

[26] C. Zhong, Y. Chen, Y. Xie, S. A. Yang, M. L. Cohen, and S. Zhang, Nanoscale **8**, 7232 (2016).

[27] Q.-F. Liang, J. Zhou, R. Yu, Z. Wang, and H. Weng, Phys. Rev. B **93**, 085427 (2016).

[28] X. M. Zhang, Z. M. Yu, Z. M. Zhu, W. K. Wu, S. S. Wang, X. L. Sheng, and S. A. Yang, Phys. Rev. B **97**, 235150 (2018).

[29] W. Wu, Y. Liu, S. Li, C. Zhong, Z.-M. Yu, X.-L. Sheng, Y. X. Zhao, and S. A. Yang, Phys. Rev. B **97**, 115125 (2018).

[30] S. Li, Z.-M. Yu, Y. Liu, S. Guan, S.-S. Wang, X. Zhang, Y. Yao, and S. A. Yang, Phys. Rev. B **96**, 081106(R) (2017).

[31] G. D. Liu, L. Jin, X. F. Dai, G. F. Chen, and X. M. Zhang, Phys. Rev. B **98**, 075157 (2018).

[32] X. M. Zhang, Z. M. Yu, Y. H. Lu, X. L. Sheng, H. Y. Yang, and S. A. Yang, Phys. Rev. B **97**, 125143 (2018).

[33] Y. Gao, Y. Chen, Y. Xie, P.-Y. Chang, M. L. Cohen, and S. Zhang, Phys. Rev. B **97**, 121108(R) (2018).

[34] Y. P. Du, F. Tang, D. Wang, L. Sheng, E.-J. Kan, C.-G. Duan, S. Y. Savrasov, and X. G. Wan, npj Quantum Mater. **2**, 3 (2017).

[35] S. Kobayashi, Y. Yamakawa, A. Yamakage, T. Inohara, Y. Okamoto, and Y. Tanaka, Phys. Rev. B **95**, 245208 (2017).

[36] X.-L. Sheng, Z.-M. Yu, R. Yu, H. Weng, and S. A. Yang, J. Phys. Chem. Lett. **8**, 3506 (2017).

[37] C. Zhong, Y. Chen, Z.-M. Yu, Y. Xie, H. Wang, S. A. Yang, and S. Zhang, Nat. Commun. **8**, 15641 (2017).

[38] W. Chen, H.-Z. Lu, and J.-M. Hou, Phys. Rev. B **96**, 041102(R) (2017).

[39] T. Bzdusek, Q. S. Wu, A. Ruegg, M. Sigrist, and A. A. Soluyanov, Nature (London) **538**, 75 (2016).

[40] G. Chang, S.-Y. Xu, X. Zhou, S.-M. Huang, B. Singh, B. Wang, I. Belopolski, J. Yin, S. Zhang, A. Bansil *et al.*, Phys. Rev. Lett. **119**, 156401 (2017).

[41] Z. Yan, R. Bi, H. Shen, L. Lu, S.-C. Zhang, and Z. Wang, Phys. Rev. B **96**, 041103(R) (2017).

[42] P.-Y. Chang and C.-H. Yee, Phys. Rev. B **96**, 081114(R) (2017).

[43] Y. Zhou, F. Xiong, X. Wan, and J. An, Phys. Rev. B **97**, 155140 (2018).

[44] H. Zhang, X. Zhang, T. He, X. Dai, Y. Liu, G. Liu, L. Wang, and Y. Zhang, Phys. Rev. B **102**, 155116 (2020).

[45] R. Kim, B.-J. Yang, and C. H. Kim, Phys. Rev. B **99**, 045130 (2019).

[46] S.-S. Wang, Y. Liu, Z.-M. Yu, X.-L. Sheng, and S. A. Yang, Nat. Commun. **8**, 1844 (2017).

[47] R. Yu, Q. Wu, Z. Fang, and H. Weng, Phys. Rev. Lett. **119**, 036401 (2017).

[48] Z. Li, Y. Xie, P.-Y. Chang, and Y. Chen, Carbon **157**, 563 (2020).

[49] C. Chen, Z. Su, X.-M. Zhang, Z. Chen, and X.-L. Sheng, J. Phys. Chem. C **51**, 121 (2017).

[50] X. Zhang, L. Jin, X. Dai, G. Chen, and G. Liu, J. Phys. Chem. Lett. **9**, 5358 (2018).

[51] A. Merkel and J. Christensen, Commun. Phys. **2**, 154 (2019).

[52] M. Xiao, X.-Q. Sun, and S. Fan, Phys. Rev. B **99**, 094206 (2019).

[53] E. Liu, Y. Sun, N. Kumar, L. Muechler, A. Sun, L. Jiao, S.-Y. Yang, D. Liu, A. Liang, Q. Xu *et al.*, Nat. Phys. **14**, 1125 (2018).

[54] D. F. Liu, A. J. Liang, E. K. Liu, Q. N. Xu, Y. W. Li, C. Chen, D. Pei, W. J. Shi, S. K. Mo, P. Dudin *et al.*, Science **365**, 1282 (2019).

[55] N. Morali, R. Batabyal, P. K. Nag, E. Liu, Q. Xu, Y. Sun, B. Yan, C. Felser, N. Avraham, and H. Beidenkopf, Science **365**, 1286 (2019).

[56] J. Yin, S. S. Zhang, G. Chang, Q. Wang, S. S. Tsirkin, Z. Guguchia, B. Lian, H. Zhou, K. Jiang, I. Belopolski *et al.*, Nat. Phys. **15**, 443 (2019).

[57] S. Chowdhury, K. F. Garrity, and F. Tavazza, npj Comput. Mater. **5**, 33 (2019).

[58] S. Borisenko, D. Evtushinsky, Q. Gibson, A. Yaresko, K. Koepernik, T. Kim, M. Ali, J. v. d. Brink, M. Hoesch, A. Fedorov *et al.*, Nat. Commun. **10**, 3424 (2019).

[59] I. Belopolski, K. Manna, D. S. Sanchez, G. Chang, B. Ernst, J. Yin, S. S. Zhang, T. Cochran, N. Shumiya, H. Zheng *et al.*, Science **365**, 1278 (2019).

[60] A. Pertsova, R. M. Geilhufe, M. Bremholm, and A. V. Balatsky, Phys. Rev. B **99**, 205126 (2019).

[61] W. Jiang, H. Huang, F. Liu, J.-P. Wang, and T. Low, Phys. Rev. B **101**, 121113(R) (2020).

[62] Y. J. Jin, R. Wang, Z. J. Chen, J. Z. Zhao, Y. J. Zhao, and H. Xu, Phys. Rev. B **96**, 201102(R) (2017).

[63] L. Jin, X. Zhang, T. He, W. Meng, X. Dai, and G. Liu, Appl. Surf. Sci. **520**, 146376 (2020).

[64] S. Nie, H. M. Weng, and F. B. Prinz, Phys. Rev. B **99**, 035125 (2019).

[65] J.-Y. You, C. Chen, Z. Zhang, X.-L. Sheng, S. A. Yang, and G. Su, Phys. Rev. B **100**, 064408 (2019).

[66] M. M. Hosen, G. Dhakal, K. Dimitri, P. Maldonado, A. Aperis, F. Kabir, C. Sims, P. Riseborough, P. M. Oppeneer, D. Kaczorowski et al., Sci. Rep. **8**, 13283 (2018).

[67] G. Chang, S.-Y. Xu, H. Zheng, B. Singh, C.-H. Hsu, G. Bian, N. Alidoust, I. Belopolski, D. S. Sanchez, S. Zhang et al., Sci. Rep. **6**, 38839 (2016).

[68] T. He, X. Zhang, W. Meng, L. Jin, X. Dai, and G. Liu, J. Mater. Chem. C **7**, 12657 (2019).

[69] J. Wang, Phys. Rev. B **96**, 081107(R) (2017).

[70] G. Xu, H. Weng, Z. Wang, X. Dai, and Z. Fang, Phys. Rev. Lett. **107**, 186806 (2011).

[71] C. Chen, Z.-M. Yu, S. Li, Z. Chen, X.-L. Sheng, and S. A. Yang, Phys. Rev. B **99**, 075131 (2019).

[72] S.-S. Wang, Z.-M. Yu, Y. Liu, Y. Jiao, S. Guan, X.-L. Sheng, and S. A. Yang, Phys. Rev. Mater. **3**, 084201 (2019).

[73] G. Kresse and D. Joubert, Phys. Rev. B **59**, 1758 (1999).

[74] P. E. Blochl, Phys. Rev. B **50**, 17953 (1994).

[75] S. Grimme, J. Comput. Chem. **27**, 1787 (2006).

[76] J. C. Gao, Q. S. Wu, C. Persson, and Z. J. Wang, arXiv:2002.04032v1.

[77] Q. S. Wu, S. N. Zhang, H.-F. Song, M. Troyer, and A. A. Soluyanov, Comput. Phys. Commun. **224**, 405 (2018).

[78] Y. Ueda, N. Fujiwara, and H. Yasuoka, J. Phys. Soc. Jpn. **66**, 778 (1997).

[79] Y. Matsushita, H. Ueda, and Y. Ueda, Nat. Mater. **4**, 845 (2005).

[80] B. Reuter and J. Jaskowsky, Angew. Chem. **72**, 209 (1960).

[81] S. Ali, M. Rashid, M. Hassan, N. A. Noor, Q. Mahmood, A. Laref, and B. U. Haq, J. Phys. B **537**, 329 (2018).

[82] S. Das, X. Zong, A. Niazi, A. Ellern, J. Q. Yan, and D. C. Johnston, Phys. Rev. B **76**, 054418 (2007).

[83] J. M. Silva, J. F. D. F. Araujob, E. Brocchi, and I. G. Solórzano, Ceram. Int. **46**, 19052 (2020).

[84] S. Karmakar and D. Behera, J. Phys.: Condens. Matter **31**, 245701 (2019).

[85] X. Feng, C. Yue, Z. Song, Q. S. Wu, and B. Wen, Phys. Rev. Mater. **2**, 014202 (2018).

[86] X. Zhang, Z.-M. Yu, X.-L. Sheng, H. Y. Yang, and S. A. Yang, Phys. Rev. B **95**, 235116 (2017).

[87] C.-J. Yi, B. Q. Lv, Q. S. Wu, B.-B. Fu, X. Gao, M. Yang, X.-L. Peng, M. Li, Y.-B. Huang, P. Richard et al., Phys. Rev. B **97**, 201107(R) (2018).

[88] J. Matsuno, A. Fujimori, and L. F. Mattheiss, Phys. Rev. B **60**, 1607 (1999).

[89] V. Eyert, K. H. Höck, S. Horn, A. Loidl, and P. S. Riseborough, Europhys. Lett. **46**, 762 (1999).

[90] I. A. Nekrasov, Z. V. Pchelkina, G. Keller, Th. Pruschke, K. Held, A. Krimmel, D. Vollhardt, and V. I. Anisimov, Phys. Rev. B **67**, 085111 (2003).

[91] D. J. Singh, P. Blaha, K. Schwarz, and I. I. Mazin, Phys. Rev. B **60**, 16359 (1999).

[92] Y. H. Zhang, J. Meng, and C. A. Taft, Mol. Phys. **107**, 1445 (2009).

[93] B. Gong, H. Yang, K. Jin, K. Liu, and Z. Lu, Chin. Phys. B **29**, 077508 (2020).

[94] A. Krimmel, A. Loidl, M. Klemm, S. Horn, and H. Schober, Phys. Rev. Lett. **82**, 2919 (1999).

[95] H. Takeda, Y. Kato, M. Yoshimura, Y. Shimizu, M. Itoh, S. Niitaka, and H. Takagi, Phys. Rev. B **92**, 045103 (2015).

[96] R. Pottgen, R.-D. Hoffmann, E. V. Sampathkumaran, I. Das, B. D. Mosel, and R. Müllmann, J. Solid State Chem. **134**, 326 (1997).

[97] E. M. Bruning, M. Brando, M. Baenitz, A. Bentien, A. M. Strydom, R. E. Walstedt, and F. Steglich, Phys. Rev. B **82**, 125115 (2010).

[98] V. Guritanu, P. Wissgott, T. Weig, H. Winkler, J. Sichelschmidt, M. Scheffler, A. Prokofiev, S. Kimura, T. Iizuka, A. M. Strydom et al., Phys. Rev. B **87**, 115129 (2013).

[99] M. Sundermann, F. Strigari, T. Willers, H. Winkler, A. Prokofiev, J. M. Ablett, J. Rueff, D. Schmitz, E. Weschke, M. M. Sala et al., Sci. Rep. **5**, 17937 (2015).

[100] P. Wissgott and K. Held, Eur. Phys. J. B **89**, 5 (2016).

[101] Y. Xu, C. Yue, H. Weng, and X. Dai, Phys. Rev. X **7**, 011027 (2017).